Article

Anomalous Metallic Phase in Molybdenum Disulphide Induced via Gate-Driven Organic Ion Intercalation

Erik Piatti *[ID], Jessica Montagna Bozzone and Dario Daghero [ID]

Department of Applied Science and Technology, Politecnico di Torino, 10129 Torino, Italy;
jessica.montagnabozzone@studenti.polito.it (J.M.B.); dario.daghero@polito.it (D.D.)
* Correspondence: erik.piatti@polito.it

Abstract: Transition metal dichalcogenides exhibit rich phase diagrams dominated by the interplay of superconductivity and charge density waves, which often result in anomalies in the electric transport properties. Here, we employ the ionic gating technique to realize a tunable, non-volatile organic ion intercalation in bulk single crystals of molybdenum disulphide (MoS_2). We demonstrate that this gate-driven organic ion intercalation induces a strong electron doping in the system without changing the pristine $2H$ crystal symmetry and triggers the emergence of a re-entrant insulator-to-metal transition. We show that the gate-induced metallic state exhibits clear anomalies in the temperature dependence of the resistivity with a natural explanation as signatures of the development of a charge-density wave phase which was previously observed in alkali-intercalated MoS_2. The relatively large temperature at which the anomalies are observed ($\sim$150 K), combined with the absence of any sign of doping-induced superconductivity down to $\sim$3 K, suggests that the two phases might be competing with each other to determine the electronic ground state of electron-doped MoS_2.

1. Introduction

Transition metal dichalcogenides (TMDs) are layered compounds where the combination of relatively simple crystal structures, complex electronic structures and electronic correlations give rise to rich phase diagrams [1], making them highly promising for fundamental investigations and potential applications alike [2,3]. Hexagonal molybdenum disulphide ($2H$-MoS_2) has been one of the most studied semiconducting TMDs owing to its chemical stability, ease of exfoliation and indirect-to-direct band gap transition in the monolayer [4–6], which make it ideally suited to the development of (opto-)electronic applications [7–9].

Upon electron doping, $2H$-MoS_2 displays a complex phase diagram as the Fermi level is tuned across its multi-valley electronic band structure [10–17]. This exploration has chiefly been enabled by the development of the ionic gating technique [18–20], which exploits the ultrahigh electric fields attainable at a voltage-polarized electrolyte–electrode interface to control the electron and/or hole doping of a material either via simple electrostatic charge induction [21–33] or more complex electrochemical effects [33–45].

Upon increasing electron doping, $2H$-MoS_2 undergoes first an insulator-to-metal transition [46–48] and, at higher doping levels, a metal-to-superconductor transition; the superconducting phase, attained both via electrostatic carrier accumulation at the surface [11,21,49,50] or electrochemical ion intercalation in the bulk [36,51,52], displays a maximum transition temperature $T_c \approx 11$ K. The highest doping levels also destabilize the $2H$-MoS_2 crystal structure, promoting the development of charge density wave (CDW) phases [37,52–56] and/or structural transitions to other polytypes [53–55,57–60].

Although, in most cases, the effects of ionic gating vanish when the gate voltage is removed, it has recently been shown that *non-volatile* charge doping of macroscopic bulk

specimens of layered crystals is attainable via gate-driven intercalation of either hydrogen [61–64] or organic ions [65]. The latter has been proven to be an effective tool to tune the electronic ground state of layered FeSe [65] and to boost its superconducting transition temperature [66,67] well beyond that achieved via other means of bulk electron doping. These results make the investigation of the effects of gate-driven organic-ion intercalation in other layered materials highly desirable.

In this work, we employ the ionic gating technique to intercalate organic ions in bulk $2H$-MoS$_2$ single crystals at room temperature. We find that the gate-induced intercalation is partially non-volatile and can be tuned by varying the amount of time during which the fully intercalated samples are kept in the ionic liquid after removal of the gate voltage.

Our organic ion-intercalated MoS$_2$ crystals retain the $2H$ crystal symmetry and undergo a doping-induced insulator-to-metal transition, with clear anomalies emerging in the temperature dependence of the resistivity around ∼150 K; all samples show no evidence of superconductivity down to ∼3 K; however, an incipient re-entrant transition to an insulating state is observed at the highest doping levels. We discuss how all the observed features can be naturally ascribed to the development of a doping-induced CDW phase assisted by disorder-induced strong localization, which may be in competition with the otherwise expected superconducting phase.

2. Materials and Methods

2.1. Electric-Field-Driven Ion Intercalation

Freshly-cleaved $2H$-MoS$_2$ crystals (SPI supplies, West Chester, PA, US; typical size 2 mm × 1 mm × 50 µm) were electrically contacted via drop-casted spots of silver paste (RS Components, Sesto San Giovanni, Italy) and immersed in a Duran crucible filled with 1-ethyl-3-methylimidazolium tetrafluoroborate ionic liquid (EMIM-BF$_4$; Merck KGaA, Darmstadt, Germany) together with a platinum (Pt) counter electrode. The setup is sketched in Figure 1a. The gate voltage V_G between the Pt electrode, and the crystal was applied by a B2961 power source (Keysight Technologies, Santa Rosa, CA, USA) at room temperature and in ambient atmosphere.

The resistivity ρ was monitored in situ by the standard four-wire method. A constant current $I_{DS} \approx 1$ µA, flowing between the drain (D) and source (S) contacts, was supplied by a 220 (Keithley, Cleveland, OH, US) current source, and the longitudinal voltage drop V_{xx} between the inner voltage contacts was measured by a 3457 multimeter (Hewlett-Packard, Palo Alto, CA, US). The resistivity was then determined as $\rho = V_{xx} I_{DS}^{-1} tw\, l^{-1}$, where t and w are the sample thickness and width, and l is the distance between the inner voltage contacts. Common-mode offsets were removed using the current-reversal method.

Open-circuit (OC) conditions were obtained by physically disconnecting the gate electrode from the power source. Ex situ characterizations were performed after extracting the intercalated MoS$_2$ samples from the cell and rinsing them thoroughly with acetone and ethanol to remove ionic-liquid residues. The samples were stored in standard desiccators either in argon atmosphere or under low vacuum to avoid moisture contamination.
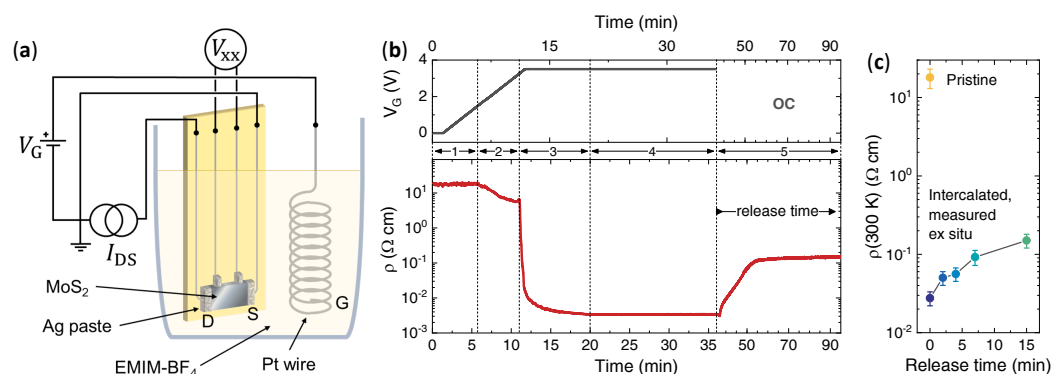
Figure 1. Electric field-driven ion intercalation. (**a**) Sketch of the ionic gating setup with the electrical connections. Source (S), drain (D) and gate (G) electrodes are explicitly highlighted. (**b**) Gate voltage (top panel) and resistivity (bottom panel) measured in situ as a function of time during a gating process. (**c**) Resistivity measured ex situ as a function of the release time.

2.2. Vibrational Spectroscopies

Both Raman and Fourier-transform infrared (FT-IR) spectra were measured on freshly-cleaved surfaces in ambient conditions. Raman spectra were acquired using an InVia H43662 micro-Raman spectrometer (Renishaw, Gloucestershire, UK). All spectra were acquired using an excitation wavelength of 514 nm, a laser power $<$ 1 mW focused through a 100X objective, an exposure time of 20 s and 50 accumulations. FT-IR spectra were measured using a Nicolet 5700 spectrometer (Thermoscientific, Waltham, MA, USA) in attenuated total reflectance (ATR) mode (Thermoscientific Smartorbit module) in the range between 900 and 3500 cm^{-1}.

The spectrum of the EMIM-BF$_4$ ionic liquid was measured by mixing the liquid with potassium bromide. The determination of the peak areas in the bands centred around $\sim$1570 and $\sim$1045 cm^{-1} in both the liquid and the intercalated MoS$_2$ samples was performed by fitting the experimental spectra in the two regions to one and four Voigt peak functions, respectively, in accordance with the peak assignments.

2.3. Nano-Infrared Microscopy

Scanning probe microscopy images were acquired on freshly-cleaved surfaces in ambient conditions by means of an Anasys nanoIR3-s atomic force microscope (AFM; Bruker, Billerica, MA, US) combined with a multichip tunable quantum cascade laser (QCL; MIRcat-QT Daylight Solutions, San Diego, CA, US) covering the IR spectral ranges 1900–1350 cm^{-1} and 1150–900 cm^{-1}, using commercial gold-coated silicon tips (Bruker PR-EX-TnIR-A). AFM topography maps were acquired in tapping mode, and the IR absorption maps were simultaneously recorded via heterodyne detection as implemented in the "Tapping AFM-IR" mode of the built-in Analysis Studio software.

All maps were acquired with $\sim$60% of the average QCL laser power (0.5 W), a duty cycle of 15% and a pulse rate $\sim$300 kHz set to allow for heterodyne detection of the IR signal amplitude. Absorption spectra were collected with a spectral resolution of 2 cm^{-1} and 64 co-averages and normalised to the QCL emission profile at the same laser power. Gwyddion software (Czech Metrology Institute, Brno, Czech Republic) [68] was employed for image analysis.

2.4. Kelvin-Probe Force Microscopy

Maps of the surface potential were acquired on freshly-cleaved surfaces in ambient conditions by means of an Innova (Bruker, Billerica, MA, US) AFM equipped with a surface potential imaging add-on, using standard platinum-iridium-covered silicon tips (Bruker SCM-PIT-V2). Pristine and intercalated samples were mounted simultaneously on the same metallic sample holder and fixed with electrically-conducting adhesive tape.

AFM topography maps were acquired in tapping mode during the forward scans, whereas Kelvin-probe force microscopy (KPFM) measurements were performed in lift mode during the backward scan by grounding the sample and biasing the KPFM tip. The $20 \times 20\,\mu\text{m}^2$ maps shown in the following were acquired using a scan rate of 0.3 Hz, a lift height of 50 nm and a tip AC bias voltage of 3 V. Gwyddion software [68] (Czech Metrology Institute, Brno, Czech Republic) was employed for image analysis.

2.5. Resistivity Measurements

The measurements of the resistivity as a function of temperature were performed in the high-vacuum chamber of a ST-403 pulse-tube cryocooler (Cryomech, Syracuse, NY, USA) with a base temperature of $\approx 2.8\,\text{K}$. The resistivity was determined with the same method employed in the room-temperature gating runs, except that I_{DS} was supplied by a B2912 (Keysight Technologies, Santa Rosa, CA, USA) source-measure unit, and V_{xx} was measured using a 34420 (Keysight Technologies, Santa Rosa, CA, USA) nanovoltmeter. In each cooling–warming cycle, only the data recorded during the slower, quasi-static warming to room temperature were considered.

3. Results

The ionic gating technique is widely employed to control the electronic properties of various classes of materials. The principle of the technique is that the material under study constitutes the active channel of an electrochemical transistor and is thus separated from a gate counter-electrode by an electrolyte, such as an ionic liquid. When polarized by the application of a finite V_{G}, the electrolyte allows the mobile ions to accumulate at the sample surface and induce an equal and opposite sheet carrier density in the channel to maintain charge neutrality, building up the electric double layer (EDL), which acts as a nanoscale capacitor with ultra-high capacitance [18–20].

The intense electric field in the EDL can then be directly exploited to electrostatically tune this surface charge density as in a conventional field-effect transistor [21–33] or to activate more complex electrochemical effects including bulk ion intercalation [33–45]. Here, we make use of the ionic gating setup sketched in Figure 1a to intercalate positively-charged organic ions in bulk 2H-MoS$_2$ crystals and induce a semi-permanent electron doping.

Figure 1b shows the resistivity ρ of a representative MoS$_2$ crystal during the gating process at room temperature. At $V_{\text{G}} = 0$, a finite $\rho \approx 18\,\Omega$ cm is measured due to the intrinsic n-doping arising from the sulphur vacancies ubiquitous in MoS$_2$ crystals [69]. As V_{G} is swept from 0 to positive values, ρ remains mostly unaffected as long as $V_{\text{G}} \lesssim +1$ V (region 1 in Figure 1b) and then starts to decrease, reaching a plateau around $\rho \approx 5.5\,\Omega$ cm in the V_{G} range between $\sim+2.75$ and $\sim+3.25$ V (region 2 in Figure 1b).

Further increasing V_{G} to $+3.5$ V then triggers a sharp decrease in ρ of about three orders of magnitude. If the gate voltage is then kept fixed at $V_{\text{G}} = +3.5$ V the resistivity saturates rather quickly ($\lesssim 10$ min, region 3 in Figure 1b) to $\rho \approx 3$ mΩ cm and shows no further change (region 4 in Figure 1b). This gate-induced change in ρ is partially volatile: when the potential difference between the Pt counter electrode and the sample is removed by setting the cell in the OC conditions (region 5 in Figure 1b), ρ rapidly increases, saturating to an intermediate value $\rho \approx 150$ mΩ cm after about 15 min; however, smaller values of ρ can be stabilized by extracting the MoS$_2$ crystal from the cell before the full OC saturation has taken place.

Figure 1c shows the ρ of gated MoS$_2$ crystals measured ex situ as a function of the release time, i.e., the time span in which each crystal has been left in the ionic liquid in OC conditions: while the lowest-resistivity state ($\rho \approx 3$ mΩ cm) observed in region 4 goes lost as soon as the gate circuit is opened, permanent modifications of the intercalated crystals leading to intermediate ρ values ranging from ≈ 25 mΩ cm up to 150 mΩ cm (and monotonically depending on the release time) can thus be obtained. With the exception of

the electric transport measurements, all characterizations have been performed on samples at zero (nominal) release time.

Since $2H$-MoS$_2$ is prone to undergo structural transitions upon heavy electron doping [54,56] and intercalation by different ionic species [53,55,57–60], the structural phase of both the pristine and the intercalated crystals was assessed via Raman spectroscopy. As shown in Figure 2a, the Raman spectrum of a pristine crystal (solid black line) exhibits the two typical modes of MoS$_2$ in the $2H$ crystal structure, the E$^1_{2g}$ mode at ∼384 cm^{-1} and the A$_{1g}$ mode at ∼409 cm^{-1}, which correspond to in-plane and out-of-plane vibrations of Mo and S atoms, respectively [11,70].

The same two peaks are also observed in the Raman spectrum of intercalated MoS$_2$ (solid red line), with no sign of the emergence of the peaks at 158, 218 and 334 cm^{-1}, which are associated with the $1T/1T'$ MoS$_2$ polytypes [57–60]. This indicates that our MoS$_2$ samples retain their $2H$ crystal structure upon EMIM intercalation.

Furthermore, Lorentzian fitting to the experimental spectra (inset to Figure 2a) indicates that the A$_{1g}$ mode undergoes a tiny ≈0.3 cm^{-1} redshift in the intercalated sample, whereas the E$^1_{2g}$ mode remains unchanged. Both features are consistent with the behaviour of MoS$_2$ nanolayers upon gate-induced electron doping [13,71,72], even though a quantitative comparison is prevented by the strong dependence of the effect on the sample thickness.
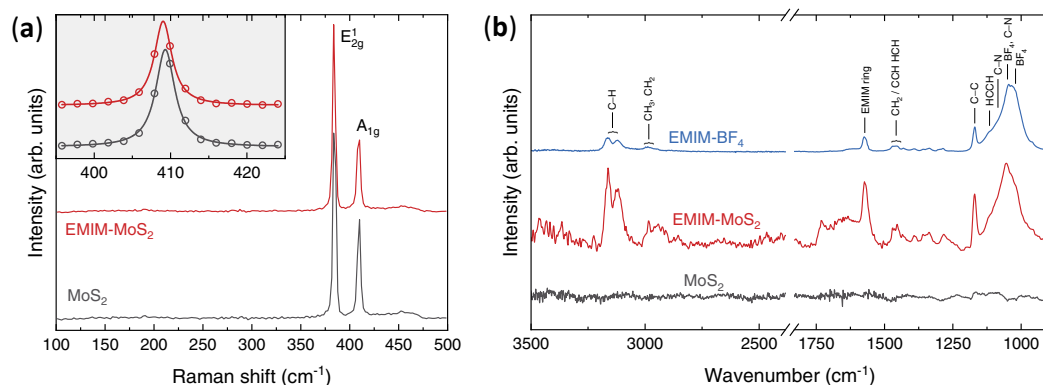

Figure 2. Vibrational spectroscopies of pristine and intercalated MoS$_2$. (**a**) Raman spectroscopy at 514 nm in the spectral range between 100 and 500 cm^{-1}, showing the E$^1_{2g}$ mode at ∼384 cm^{-1} and the A$_{1g}$ mode at ∼409 cm^{-1}. Inset shows a magnification of the data in the A$_{1g}$ region close to 409 cm^{-1}. Solid lines are Lorentzian fits. (**b**) FT-IR absorption spectra acquired in ATR mode between 3500 and 900 cm^{-1}. Peak assignments for the spectrum of EMIM-BF$_4$ are indicated.

The successful incorporation of EMIM ions in the MoS$_2$ lattice was confirmed by FT-IR measurements. As shown in Figure 2b, the infrared spectrum of the pristine MoS$_2$ crystal (solid black line) is mostly featureless in the investigated frequency ranges, since the sharp infrared peaks typical of the $2H$ phase emerge at wavenumbers below ∼500 cm^{-1} [73]. Conversely, the spectrum of the intercalated MoS$_2$ sample (solid red line) exhibits several bands, that are actually typical of organic compounds. Indeed, they fall in the C–H stretching region (between 3200 and 2800 cm^{-1}) and in the fingerprint region (between 1800 and 900 cm^{-1}).

Notably, the same bands are also observed in the spectrum of the EMIM-BF$_4$ ionic liquid (solid blue line). In accordance with the literature, we assign the structure between 3200 and 3050 cm^{-1} to the C–H stretching modes involving unsaturated C atoms in the EMIM ring [74–76]; the band between 3000 and 2850 cm^{-1} to the aliphatic C–H modes of the CH$_3$ group bonded to the EMIM ring, the CH$_3$ terminal group of the ethyl chain and the CH$_2$ group [74–76]; the peak around 1572 cm^{-1} to the EMIM-ring breathing [74–76]; the band around 1450 cm^{-1} to the (CH$_2$)/CCH HCH bending modes [74–76]; the peak around 1170 cm^{-1} to the C–C aliphatic stretching modes [74–76].

All these bands are associated purely to the EMIM cation. Conversely, the broad band between 1150 and 900 cm^{-1} comprises at least four peaks arising both from the cation and the BF$_4$ anion. Specifically, we assign the peak around 1116 cm^{-1} to ring HCCH symmetric bending [75,76]; the peak around 1085 cm^{-1} to C–N stretching [75]; the peak around 1050 cm^{-1} to a combination of BF$_4$ asymmetric stretching and C–N symmetric stretching [76]; and the peak around 1021 cm^{-1} to BF$_4$ asymmetric stretching [75,76]. As such, only this last peak can be uniquely associated with the presence of the BF$_4$ anion.

The fact that all the main absorption bands of the EMIM-BF$_4$ ionic liquid are observed also in the infrared spectrum of the intercalated MoS$_2$ sample indicates that both the EMIM cation and the BF$_4$ anion are incorporated in the MoS$_2$ lattice. However, the relative intensity of the BF$_4$-related bands with respect to that of the EMIM-related ones is much lower in the intercalated MoS$_2$ sample than in the ionic liquid.

Specifically, the peak-area ratio between the BF$_4$-stretching mode at ~1021 cm^{-1} and the EMIM-breathing mode at ~1572 cm^{-1} in the EMIM-BF$_4$ ionic liquid ($A_{\mathrm{BF_4}}/A_{\mathrm{EMIM}} \approx 12$) is about 10-times larger than that in the intercalated MoS$_2$ sample ($A_{\mathrm{BF_4}}/A_{\mathrm{EMIM}} \approx 1.2$). Considering that the ionic liquid has a 1:1 EMIM:BF$_4$ stoichiometry, this allows us to estimate that in the intercalated MoS$_2$ samples about one BF$_4$ anion every ~10 EMIM cations is incorporated in the lattice as a contaminant. The fact that the MoS$_2$ lattice incorporates a much larger amount of cations than of anions confirms a net electron doping in the intercalated samples.

The spatial distribution of the intercalants was investigated by nanoscale infrared spectroscopy [77,78]. Figure 3a shows a $20 \times 20\,\mu\text{m}^2$ AFM topography map of a freshly-cleaved MoS$_2$ crystal. Unlike the nearly atomically-flat surface of pristine crystals (discussed later), intercalated MoS$_2$ exhibits a somewhat corrugate surface (RMS roughness $S_q \approx 15$ nm), although atomically-flat terraces can still be observed.

Furthermore, much taller (≈ 200 nm) ellipsoidal features are randomly scattered on top of the surface and exhibit a strong contrast in the tapping phase image (Figure 3b), which indicates that their mechanical properties differ significantly from those of the MoS$_2$ background. IR absorption spectra were then collected both on one of these "droplets" (point D) and on the exposed surface (point S). As shown in Figure 3b, both spectra display the peaks, specific of the EMIM cation, at about 1572 cm^{-1}, 1450 cm^{-1} and 1170 cm^{-1}, as well as the broad band between 1150 and 900 cm^{-1}, which also includes the BF$_4$-related peak at ~1021 cm^{-1}.

However, in the spectrum acquired on the droplet (solid blue line) this latter band is much more pronounced than the EMIM-related peaks, as it happens in the FT-IR spectrum of the pure ionic liquid shown in Figure 2b. Conversely, in the spectrum acquired on the exposed MoS$_2$ surface, the BF$_4$-related band is significantly less intense with respect to the EMIM-related peaks: in particular, the spectral weight of the BF$_4$-stretching peak at ~1021 cm^{-1} is strongly suppressed.

Combined with the phase contrast, these results strongly suggest that the droplets are due to ionic-liquid residues embedded within the MoS$_2$ planes (and exposed to the surface after cleaving), and their presence is the main source of BF$_4$ anions detected by FT-IR. Finally, the spatial distribution of the intercalated EMIM cations was studied by acquiring an IR absorption map in correspondence of the EMIM-breathing mode at ~1572 cm^{-1}. As shown in Figure 3d, a finite IR absorption at this wavenumber can be observed throughout the entire surface, and it is notably minimum in the areas covered by the ionic-liquid residues. However, a long-range modulation in the IR absorption over a length scale ~10 μm can be distinguished, which indicates that EMIM incorporation in the MoS$_2$ lattice is inhomogeneous and develops local minima and maxima over a comparable length scale.

The impact of the EMIM intercalation on the electronic structure of MoS$_2$ was assessed by means of Kelvin-probe force microscopy [79–81] on a pristine MoS$_2$ crystal and on the same intercalated crystal characterized via nano-IR. Figure 4a and b show the AFM topography map and surface potential distribution of the pristine MoS$_2$, respectively. As

expected for the cleaved surface of a layered material, the topography is flat ($S_q \approx 1.5$ nm), atomic steps and terraces can be distinguished, and the surface potential is featureless and nearly homogeneous across the entire area.

The topography map of intercalated MoS_2 (Figure 4c) again exhibits a much larger background corrugation ($S_q \approx 15$ nm) and the localized features associated with ionic-liquid contaminants. More importantly, the surface potential of intercalated MoS_2 (Figure 4d) is inhomogeneous and exhibits fluctuations over the same length scale (~ 10 μm) that characterizes the fluctuations in the EMIM content detected via nanoIR.

As clearly shown by the direct comparison of the histograms of the two images reported in Figure 4e, the surface potential of intercalated MoS_2 is also shifted to lower values with respect to that of pristine MoS_2 across the entire area. This reduction in surface potential is a direct proof of electron doping due to the insertion of the EMIM cations in the MoS_2 lattice, since it signifies that in the intercalated MoS_2, the Fermi level has been shifted upwards in energy and closer to the vacuum level.
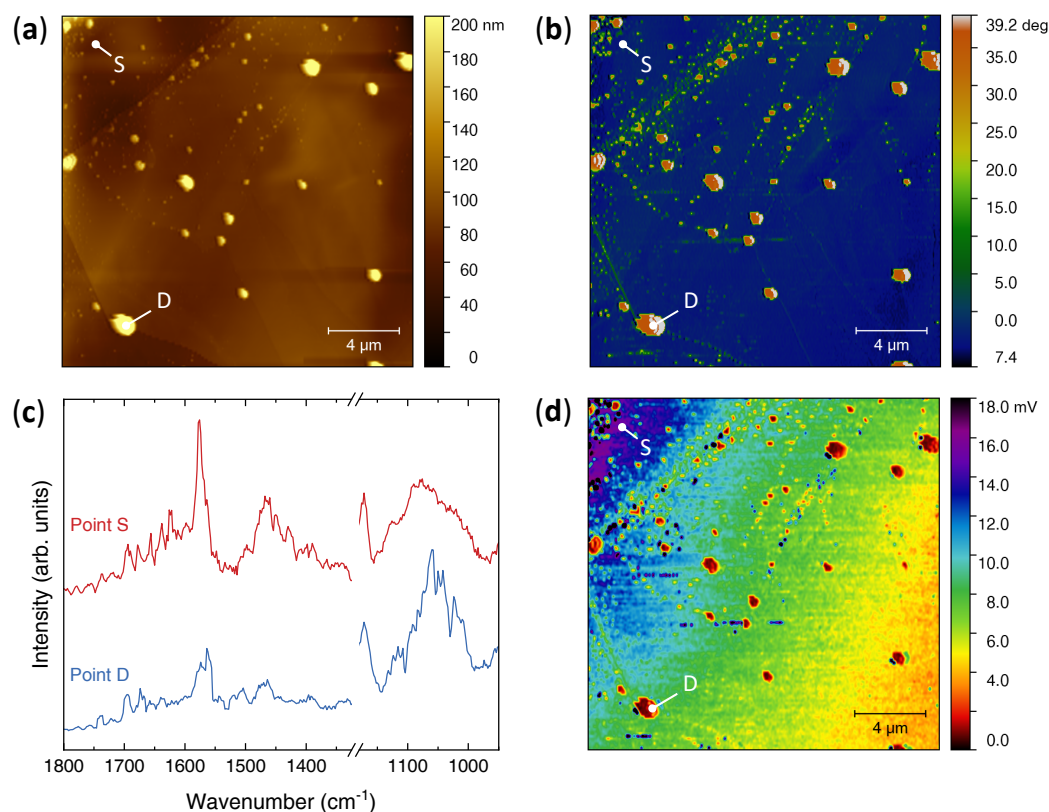

Figure 3. Infrared nanospectroscopy of intercalated MoS_2. (**a**) AFM topography map. (**b**) Phase image of the same area. (**c**) nano-IR absorption spectra acquired in correspondence of a droplet (solid blue line, point D) and of the MoS_2 exposed surface (solid red line, point S). (**d**) IR absorption map of the same area acquired in correspondence of the EMIM-breathing mode at ~ 1572 cm^{-1}.
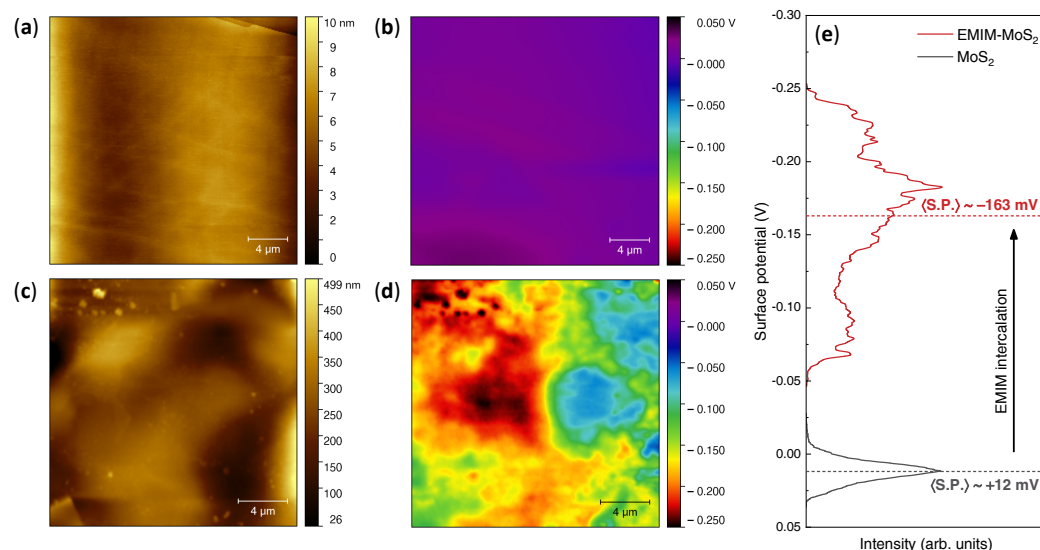
Figure 4. Kelvin-probe force microscopy of pristine and intercalated MoS_2. (**a**) AFM topography map of pristine MoS_2. (**b**) Surface potential map of pristine MoS_2. (**c**) AFM topography map of intercalated MoS_2. (**d**) Surface potential map of intercalated MoS_2. (**e**) Surface potential histograms highlighting the shift in the Fermi energy induced by the intercalation of EMIM ions.

The average shift in Fermi energy ΔE_F between the two systems can then be estimated simply as:

$$\Delta E_F = -e\left(\langle S.P.\rangle_{\text{intercalated}} - \langle S.P.\rangle_{\text{pristine}}\right) = 175\,\text{meV} \tag{1}$$

where e is the elementary charge, $\langle S.P.\rangle_{\text{pristine}} = +12$ mV and $\langle S.P.\rangle_{\text{intercalated}} = -163$ mV are the average values of the surface potential in pristine and intercalated MoS_2, respectively. From this shift in the Fermi energy, the average density of electrons n_e doped into the conduction band of MoS_2 can also be determined, since the Fermi level of pristine MoS_2 is known to be pinned to the bottom of the conduction band by the presence of sulphur vacancies in the crystal [69]. In particular, assuming a parabolic three-dimensional dispersion of the density of states of bulk MoS_2:

$$n_e = \frac{\nu_s \nu_v}{6\pi^2}\left(\frac{2m^*}{\hbar^2}\Delta E_F\right)^{\frac{3}{2}} \tag{2}$$

with a spin degeneracy $\nu_s = 2$, a valley degeneracy $\nu_v = 6$ [47,82] and an effective mass $m^* = 0.6m_e$ [82], one obtains $n_e \sim 9 \times 10^{20}$ cm^{-3}. If every intercalated EMIM cation were to donate one electron to the MoS_2 conduction band, this would correspond to about one EMIM cation every ~ 20 MoS_2 formula units, or a nominal stoichiometry of $EMIM_{0.05}MoS_2$.

Having established the mechanism and amount of electron doping provided by the EMIM intercalation in the MoS_2 crystals, we now turn to consider how this affects their electric transport properties as a function of temperature T. Figure 5a shows the T-dependence of ρ, divided by its value at $T = 300$ K (shown in Figure 1c), down to $T \sim 3$ K and for a series of MoS_2 crystals with increasing release times. The pristine MoS_2 crystal shows the exponentially-increasing ρ with decreasing T typical of insulators where conduction occurs via hopping processes in the localized states in the band tails, as expected [48,69].

The T-dependence of ρ in the intercalated samples is much less steep, and its values at low T are several orders of magnitude lower than that of pristine MoS_2, consistent with a metallization induced by the electron doping. A closer inspection of the curves for the intercalated samples (Figure 5b) reveals a complex dependency of ρ on both T and release time. The sample at zero release time exhibits an overall metallic behaviour, in the sense that its ρ decreases on going from 300 K to 3 K; however, this T-dependence is not monotonic, and a clear anomaly can be observed in the form of a broad hump appearing between 50 and 150 K.

This behaviour is best visualized by plotting the first derivative of ρ with respect to T, $d\rho/dT$. As shown in Figure 5c, this anomaly gives rise to a hump-dip structure in the T-dependence of $d\rho/dT$, with a broad hump at lower T and a sharp dip at higher T, the latter being highlighted by the dashed lines. Additionally, a small resistance upturn is observed for $T \lesssim 20$ K, indicating that at low T, some degree of carrier localization is present in the sample.

We tracked the evolution of these two main features—the degree of metallicity and resistivity anomaly—on the increasing release time by defining two distinct figures of merit: for the metallicity, the residual resistivity ratio RRR, defined as usual as $\rho(300\,\text{K})/\rho(3\,\text{K})$; for the resistivity anomaly, the temperature T^* where the dip in $d\rho/dT$ is located. Figure 5d shows that, upon increasing the release time (i.e., decreasing the electron doping), T^* (violet circles, left scale) decreases in a nearly monotonic fashion from $\sim$155 K at release times below $\sim$2 min, to $\sim$115 K at release times $\gtrsim$ 15 min.

At the same time, however, RRR (green diamonds, right scale) exhibits a clearly non-monotonic trend: after an initial increase from $\sim$2.7 to $\sim$5.7 for release times $\lesssim$ 4 min, it strongly decreases down to $\sim$0.58 at release times $\gtrsim$15 min, i.e., when spontaneous deintercalation of the EMIM ions stops. This indicates that the intercalation stage obtained with a release time of 4 min achieves a maximum degree of metallicity, and doping the sample away from it shifts the system towards an insulating behaviour.
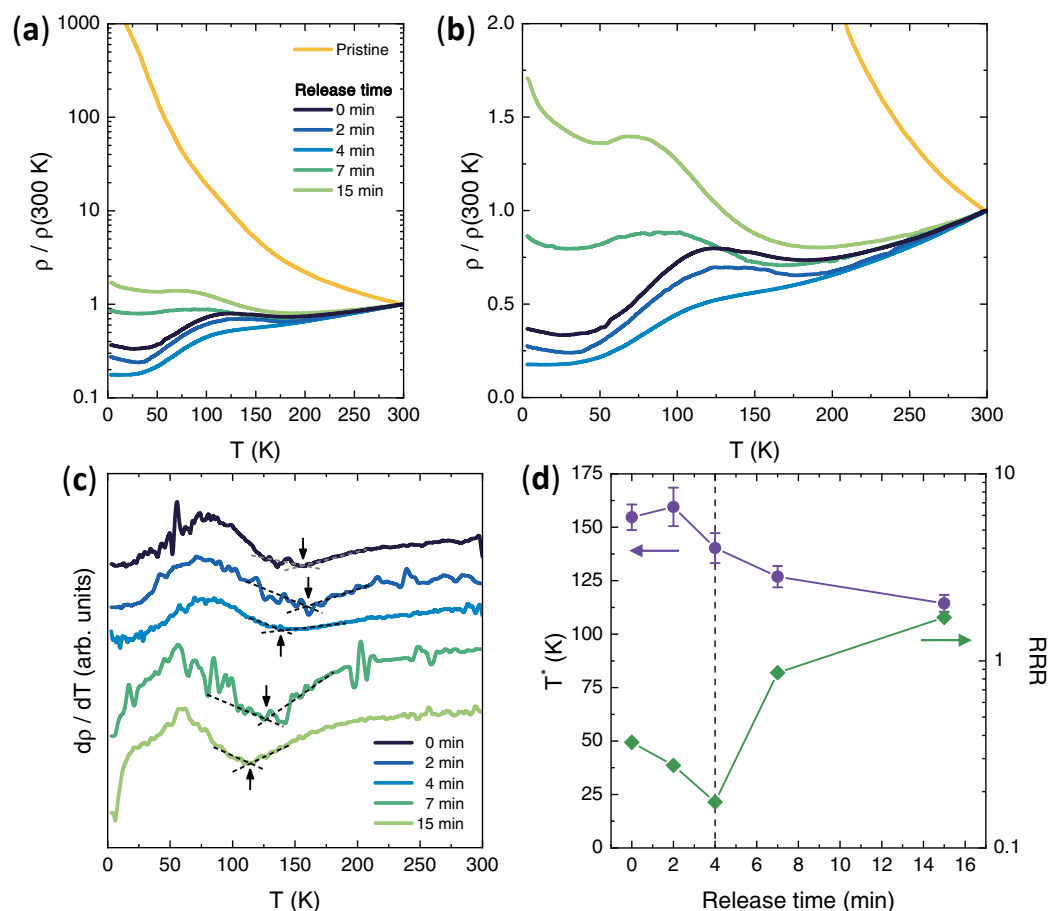

Figure 5. Temperature dependence of the electric transport in pristine and intercalated MoS$_2$. (**a**) Resistivity ρ divided by its value at 300 K as a function of temperature T, before and after EMIM intercalation, in semi-logarithmic scale. (**b**) same as in (**a**) but on a linear scale. (**c**) T dependence of $d\rho/dT$, before and after EMIM intercalation, obtained by numerical derivation of the curves in (**b**). Arrows highlight the values of T where $d\rho/dT$ shows a dip (T^*). The curves are vertically offset for clarity. (**d**) T^* (violet circles, left scale) and residual resistivity ratio ρ (green diamonds, right scale) as a function of the release time.

4. Discussion

In our EMIM-intercalated MoS_2 crystals, increasing the release time reduces the doping and therefore brings the samples back toward the MoS_2 pristine state of a band insulator. On the other side, reducing the release time increases the doping level and brings the samples closer to an insulating state that, however, must have a different origin, since increasing the concentration of EMIM dopants should, in principle, provide a larger density of free electrons to the conduction band. Such insulating state must, therefore, be due to some kind of localization.

A first source of localization could be the randomness caused by intercalation and progressive introduction of disorder in the form of extra scattering centres due to the presence of the ions themselves [36,83–87]: this type of gate-driven re-entrant transition (from a band insulator, to a metal and finally to an Anderson insulator) has already been reported in other ion-gated TMDs [88–90] and oxides [42].

A second source of localization could instead be associated with the same phenomenon giving rise to the resistivity anomaly, which is often found among TMDs and represents one of the typical signatures of the onset of CDW phases [1]. These consist of a periodic modulation of the charge carrier density accompanied by a distortion of the underlying crystal lattice [91], usually resulting from strong electron-phonon coupling [92] and/or Fermi-surface nesting [93].

CDW phases are susceptible to charge carrier doping: in most TMD compounds, CDWs are suppressed by increasing doping in favour of the development of superconducting phases [28,34,94–96]; however, in some specific compounds, the CDW order is instead promoted by doping [26,37,52].

Density functional theory calculations predicted $2H$-MoS_2 to fall into the latter category, both in the bulk [53,55] and in the monolayer [54,56] form. Recent experimental evidences have confirmed that, indeed, the onset of a CDW order in MoS_2 bulk crystals and bulk-like flakes is promoted by Li-doping [37] and K-doping [52], as well as by pressure [97]. In this context, T^* would mark the critical temperature for the CDW phase transition in EMIM-intercalated MoS_2, placing it in an intermediate range between those of Li_xMoS_2 ($\approx$230 K) and K_xMoS_2 ($\approx$85 K).

The onset of CDW order can naturally explain why resistivity anomalies emerge in our EMIM-intercalated MoS_2 crystals and can also provide an additional possible mechanism for the observed incipient localization at high doping, i.e., the opening of a (possibly partial) gap on the Fermi surface associated with the CDW [52,55]. It is interesting, at this stage, to understand the reasons why superconductivity is not observed in MoS_2, at least down to 2.8 K, upon EMIM intercalation. The fact is that both Li-doping and K-doping instead lead to the appearance of a superconducting phase, although with certain differences.

In K-intercalated MoS_2, where the CDW order sets in at a low T^*, bulk superconductivity occurs with a critical temperature $T_c \approx 7$ K [51,52] throughout most of its phase diagram with little change in T_c as a function of the K content (between $K_{0.13}MoS_2$ and $K_{1.5}MoS_2$) [51]. In Li-intercalated MoS_2, where T^* is high, superconductivity (with $T_c \approx 3.7$ K) is observed only in samples showing no sign of CDW-related resistivity anomalies [36].

In our EMIM-intercalated crystals, in which the CDW order is ubiquitous but sets in at intermediate temperatures T^*, no sign of superconductivity has been detected. One could object that the range of doping contents of our samples may not be the right range to observe superconductivity. This is certainly possible; however, since the EMIM doping distribution is largely inhomogeneous, the system actually experiences a wide range of local electron doping levels, from small ones to others that are much larger than the highest average doping content calculated above.

This means that, if there were a sufficiently wide range of doping for superconductivity to develop, at least a fraction of the volume should fall in that range. Even if this fraction were not sufficient to ensure superconducting percolation, a reduction in the resistivity should be observed. The fact that this does not happen suggests that the superconducting phase either does not develop at all or, if it does, has a low T_c (smaller than 2.8 K).

This whole picture appears to indicate that the CDW order is competing with superconductivity in MoS_2, and thus the superconducting phase appears with higher T_c only when the CDW is suppressed or at least T^* is lower. Alternatively, the lack of superconductivity in EMIM-intercalated MoS_2 could be due to the large size of the organic ions, which strongly increases the interlayer spacing: this would make the intercalated system akin to a stack of electronically-decoupled MoS_2 monolayers, where superconductivity occurs with a much lower $T_c \lesssim 2$ K and is much more easily suppressed by disorder [98,99].

Such decoupling was reported in the case of another TMD compound when intercalated via organic molecules, $SnSe_2$, where the electronic decoupling was shown to increase the superconducting T_c [100,101]. Overall, which of the depicted scenarios—or combination thereof—is at the origin of the anomalous metallic transport exhibited by our EMIM-intercalated MoS_2 crystals is left as an open question, making future investigations highly desirable.

Electric transport measurements below $\sim$3 K would of course be needed to ascertain whether superconductivity develops at lower temperatures than those achievable in the setup used in the current study. Moreover, low-temperature structure-sensitive techniques, such as Raman spectroscopy, X-ray diffraction and scanning tunnelling microscopy, would be highly beneficial to provide direct evidence for CDW ordering in the system, as well as to track its evolution as a function of temperature and doping.

5. Conclusions

In summary, we synthesized organic ion-intercalated molybdenum disulphide crystals via the ionic gating method with EMIM-BF_4 ionic liquid. We showed that the intercalation is partially non-volatile and can be tuned by allowing spontaneous de-intercalation to occur when the crystals are left in the electrochemical cell in open-circuit conditions. By combining vibrational spectroscopies, Kelvin-probe force microscopy and nano-infrared microscopy, we demonstrated that the EMIM ions act as electron donors and are intercalated in the entire sample volume with their density exhibiting fluctuations over a length scale of the order of $\sim$10 µm.

We characterized the temperature dependence of the resistivity in the intercalated crystals, showing how increasing EMIM intercalation drives the system across a re-entrant insulator-to-metal transition, i.e., from the pristine band insulator into an anomalous metallic state and eventually towards an incipient second insulating state. We further revealed the appearance of a doping-induced hump in the resistivity around $\sim$150 K, which we attribute to the development of a charge-density wave phase on the basis of the established literature on Li-doped and K-doped MoS_2. A qualitative comparison between these three systems, in particular focused on the relation between the appearance of superconductivity and the onset of the charge-density-wave phase, is suggestive of competition between these two quantum phases in electron-doped MoS_2.

Author Contributions: Conceptualization, E.P.; methodology, E.P.; investigation, E.P. and J.M.B.; resources, D.D.; data curation, E.P. and J.M.B.; writing—original draft preparation, E.P.; writing—review and editing, E.P. and D.D.; visualization, E.P.; supervision, D.D.; project administration, D.D.; funding acquisition, D.D. All authors have read and agreed to the published version of the manuscript.

Institutional Review Board Statement: Not applicable.

Informed Consent Statement: Not applicable.

Data Availability Statement: All data needed to evaluate the conclusions in the paper are included in the manuscript. Additional data related to this paper may be obtained from the corresponding author upon reasonable request.

Conflicts of Interest: The authors declare no conflict of interest. The funders had no role in the design of the study; in the collection, analyses or interpretation of data; in the writing of the manuscript; or in the decision to publish the results.

References

1. Klemm, R.A. Pristine and intercalated transition metal dichalcogenide superconductors. *Physica C* **2015**, *514*, 86–94. https://doi.org/10.1016/j.physc.2015.02.023.

2. Manzeli, S.; Ovchinnikov, D.; Pasquier, D.; Yazyev, O.V.; Kis, A. 2D transition metal dichalcogenides. *Nat. Rev. Mater.* **2017**, *2*, 17033. https://doi.org/10.1038/natrevmats.2017.33.

3. Choi, W.; Choudhary, N.; Han, G.H.; Park, J.; Akinwande, D.; Lee, Y.H. Recent development of two-dimensional transition metal dichalcogenides and their applications. *Mater. Today* **2017**, *20*, 116–130. https://doi.org/10.1016/j.mattod.2016.10.002.

4. Mak, K.F.; Lee, C.; Hone, J.; Shan, J.; Heinz, T.F. Atomically thin MoS_2: A new direct-gap semiconductor. *Phys. Rev. Lett.* **2010**, *105*, 136805. https://doi.org/10.1103/PhysRevLett.105.136805.

5. Splendiani, A.; Sun, L.; Zhang, Y.; Li, T.; Kim, J.; Chim, C.Y.; Galli, G.; Wang, F. Emerging photoluminescence in monolayer MoS_2. *Nano Lett.* **2010**, *10*, 1271–1275. https://doi.org/10.1021/nl903868w.

6. Wang, Q.H.; Kalantar-Zadeh, K.; Kis, A.; Coleman, J.N.; Strano, M.S. Electronics and optoelectronics of two-dimensional transition metal dichalcogenides. *Nat. Nanotechnol.* **2012**, *7*, 699–712. https://doi.org/10.1038/nnano.2012.193.

7. Schaibley, J.R.; Yu, H.; Clark, G.; Rivera, P.; Ross, J.S.; Seyler, K.L.; Yao, W.; Xu, X. Valleytronics in 2D materials. *Nat. Rev. Mater.* **2016**, *1*, 16055. https://doi.org/10.1038/natrevmats.2016.55.

8. Ferrari, A.C.; Bonaccorso, F.; Fal'Ko, V.; Novoselov, K.S.; Roche, S.; Bøggild, P.; Borini, S.; Koppens, F.H.; Palermo, V.; Pugno, N.; et al. Science and technology roadmap for graphene, related two-dimensional crystals, and hybrid systems. *Nanoscale* **2015**, *7*, 4598–4810. https://doi.org/10.1039/C4NR01600A.

9. Mak, K.F.; Shan, J. Photonics and optoelectronics of 2D semiconductor transition metal dichalcogenides. *Nat. Photon.* **2016**, *10*, 216–226. https://doi.org/10.1038/nphoton.2015.282.

10. Ge, Y.; Liu, A.Y. Phonon-mediated superconductivity in electron-doped single-layer MoS_2: A first-principles prediction. *Phys. Rev. B* **2013**, *87*, 241408(R). https://doi.org/10.1103/PhysRevB.87.241408.

11. Piatti, E.; De Fazio, D.; Daghero, D.; Tamalampudi, S.R.; Yoon, D.; Ferrari, A.C.; Gonnelli, R.S. Multi-valley superconductivity in ion-gated MoS_2 layers. *Nano Lett.* **2018**, *18*, 4821–4830. https://doi.org/10.1021/acs.nanolett.8b01390.

12. Piatti, E.; Romanin, D.; Gonnelli, R.S. Mapping multi-valley Lifshitz transitions induced by field-effect doping in strained MoS_2 nanolayers. *J. Phys. Condens. Matter* **2019**, *31*, 114002. https://doi.org/10.1088/1361-648X/aaf981.

13. Sohier, T.; Ponomarev, E.; Gibertini, M.; Berger, H.; Marzari, N.; Ubrig, N.; Morpurgo, A.F. Enhanced electron-phonon interaction in multivalley materials. *Phys. Rev. X* **2019**, *9*, 031019. https://doi.org/10.1103/PhysRevX.9.031019.

14. Garcia-Goiricelaya, P.; Lafuente-Bartolome, J.; Gurtubay, I.G.; Eiguren, A. Long-living carriers in a strong electron–phonon interacting two-dimensional doped semiconductor. *Commun. Phys.* **2019**, *2*, 81. https://doi.org/10.1038/s42005-019-0182-0.

15. Romanin, D.; Brumme, T.; Daghero, D.; Gonnelli, R.S.; Piatti, E. Strong band-filling-dependence of the scattering lifetime in gated MoS_2 nanolayers induced by the opening of intervalley scattering channels. *J. Appl. Phys.* **2021**, *128*, 063907. https://doi.org/10.1063/5.0017921.

16. Garcia-Goiricelaya, P.; Lafuente-Bartolome, J.; Gurtubay, I.G.; Eiguren, A. Emergence of large nonadiabatic effects induced by the electron-phonon interaction on the complex vibrational quasiparticle spectrum of doped monolayer MoS_2. *Phys. Rev. B* **2020**, *101*, 054304. https://doi.org/10.1103/PhysRevB.101.054304.

17. Pimenta Martins, L.G.; Carvalho, B.R.; Occhialini, C.A.; Neme, N.P.; Park, J.H.; Song, Q.; Venezuela, P.; Mazzoni, M.S.C.; Matos, M.J.S.; Kong, J.; et al. Electronic Band Tuning and Multivalley Raman Scattering in Monolayer Transition Metal Dichalcogenides at High Pressures. *ACS Nano*, 2022, *In press*. https://doi.org/10.1021/acsnano.2c01065.

18. Fujimoto, T.; Awaga, K. Electric-double-layer field-effect transistors with ionic liquids. *Phys. Chem. Chem. Phys.* **2013**, *15*, 8983. https://doi.org/10.1039/c3cp50755f.

19. Ueno, K.; Shimotani, H.; Yuan, H.; Ye, J.; Kawasaki, M.; Iwasa, Y. Field-Induced Superconductivity in Electric Double Layer Transistors. *J. Phys. Soc. Jpn.* **2014**, *83*, 032001. https://doi.org/10.7566/JPSJ.83.032001.

20. Liu, P.; Lei, B.; Chen, X.; Wang, L.; Wang, X. Superior carrier tuning in ultrathin superconducting materials by electric-field gating. *Nat. Rev. Phys.* **2022**, *4*, 336–352. https://doi.org/10.1038/s42254-022-00438-2.

21. Ye, J.T.; Zhang, Y.J.; Akashi, R.; Bahramy, M.S.; Arita, R.; Iwasa, Y. Superconducting dome in a gate-tuned band insulator. *Science* **2012**, *338*, 1193–1196. https://doi.org/10.1126/science.1228006.

22. Piatti, E. Ionic gating in metallic superconductors: A brief review. *Nano Ex.* **2021**, *2*, 024003. https://doi.org/10.1088/2632-959X/ac011d.

23. Ye, J.T.; Inoue, S.; Kobayashi, K.; Kasahara, Y.; Yuan, H.T.; Shimotani, H.; Iwasa, Y. Liquid-gated interface superconductivity on an atomically flat film. *Nat. Mater.* **2010**, *9*, 125–128. https://doi.org/10.1038/nmat2587.

24. Jo, S.; Costanzo, D.; Berger, H.; Morpurgo, A.F. Electrostatically induced superconductivity at the surface of WS_2. *Nano Lett.* **2015**, *15*, 1197–1202. https://doi.org/10.1021/nl504314c.

25. Piatti, E.; Daghero, D.; Ummarino, G.A.; Laviano, F.; Nair, J.R.; Cristiano, R.; Casaburi, A.; Portesi, C.; Sola, A.; Gonnelli, R.S. Control of bulk superconductivity in a BCS superconductor by surface charge doping via electrochemical gating. *Phys. Rev. B* **2017**, *95*, 140501(R). https://doi.org/10.1103/PhysRevB.95.140501.

26. Xi, X.; Berger, H.; Forró, L.; Shan, J.; Mak, K.F. Gate tuning of electronic phase transitions in two-dimensional NbSe$_2$. *Phys. Rev. Lett.* **2016**, *117*, 106801. https://doi.org/10.1103/PhysRevLett.117.106801.

27. Piatti, E.; Romanin, D.; Daghero, D.; Gonnelli, R.S. Two-dimensional hole transport in ion-gated diamond surfaces: A brief review. *Low Temp. Phys.* **2019**, *45*, 1143–1155. https://doi.org/10.1063/10.0000122.

28. Li, L.J.; O'Farrell, E.C.T.; Loh, K.P.; Eda, G.; Özyilmaz, B.; Castro Neto, A.H. Controlling many-body states by the electric-field effect in a two-dimensional material. *Nature* **2016**, *529*, 185–189. https://doi.org/10.1038/nature16175.

29. Lei, B.; Cui, J.H.; Xiang, Z.J.; Shang, C.; Wang, N.Z.; Ye, G.J.; Luo, X.G.; Wu, T.; Sun, Z.; Chen, X.H. Evolution of high-temperature superconductivity from a low-T c phase tuned by carrier concentration in FeSe thin flakes. *Phys. Rev. Lett.* **2016**, *116*, 077002. https://doi.org/10.1103/PhysRevLett.116.077002.

30. Piatti, E.; Galanti, F.; Pippione, G.; Pasquarelli, A.; Gonnelli, R.S. Towards the insulator-to-metal transition at the surface of ion-gated nanocrystalline diamond films. *Eur. Phys. J. Spec. Top.* **2019**, *228*, 689–696. https://doi.org/10.1140/epjst/e2019-800188-9.

31. Wang, Z.; Zhang, T.; Ding, M.; Dong, B.; Li, Y.; Chen, M.; Li, X.; Huang, J.; Wang, H.; Zhao, X.; et al. Electric-field control of magnetism in a few-layered van der Waals ferromagnetic semiconductor. *Nat. Nanotechnol.* **2018**, *13*, 554–559. https://doi.org/10.1038/s41565-018-0186-z.

32. Piatti, E.; Pasquarelli, A.; Gonnelli, R.S. Orientation-dependent electric transport and band filling in hole co-doped epitaxial diamond films. *Appl. Surf. Sci.* **2020**, *528*, 146795. https://doi.org/10.1016/j.apsusc.2020.146795.

33. Shi, W.; Ye, J.; Zhang, Y.; Suzuki, R.; Yoshida, M.; Miyazaki, J.; Inoue, N.; Saito, Y.; Iwasa, Y. Superconductivity series in transition metal dichalcogenides by ionic gating. *Sci. Rep.* **2015**, *5*, 12534. https://doi.org/10.1038/srep12534.

34. Yu, Y.; Yang, F.; Lu, X.F.; Yan, Y.J.; Cho, Y.H.; Ma, L.; Niu, X.; Kim, S.; Son, Y.W.; Feng, D.; et al. Gate-tunable phase transitions in thin flakes of 1T-TaS$_2$. *Nat. Nanotechnol.* **2015**, *10*, 270–276. https://doi.org/10.1038/nnano.2014.323.

35. Shiogai, J.; Ito, Y.; Mitsuhashi, T.; Nojima, T.; Tsukazaki, A. Electric-field-induced superconductivity in electrochemically etched ultrathin FeSe films on SrTiO$_3$ and MgO. *Nat. Phys.* **2016**, *12*, 42–46. https://doi.org/10.1038/nphys3530.

36. Piatti, E.; Chen, Q.; Ye, J. Strong dopant dependence of electric transport in ion-gated MoS$_2$. *Appl. Phys. Lett.* **2017**, *111*, 013106. https://doi.org/10.1063/1.4992477.

37. Piatti, E.; Chen, Q.; Tortello, M.; Ye, J.; Gonnelli, R.S. Possible charge-density-wave signatures in the anomalous resistivity of Li-intercalated multilayer MoS$_2$. *Appl. Surf. Sci.* **2018**, *461*, 269–275. https://doi.org/10.1016/j.apsusc.2018.05.232.

38. Ying, T.P.; Wang, M.X.; Wu, X.X.; Zhao, Z.Y.; Zhang, Z.Z.; Song, B.Q.; Li, Y.C.; Lei, B.; Li, Q.; Yu, Y.; et al. Discrete superconducting phases in FeSe-derived superconductors. *Phys. Rev. Lett.* **2018**, *121*, 207003. https://doi.org/10.1103/PhysRevLett.121.207003.

39. Jeong, J.; Aetukuri, N.; Graf, T.; Schladt, T.D.; Samant, M.G.; Parkin, S.S.P. Suppression of metal-insulator transition in VO$_2$ by electric field–induced oxygen vacancy formation. *Science* **2013**, *339*, 1402–1405. https://doi.org/10.1126/science.1230512.

40. Li, M.; Han, W.; Jiang, X.; Jeong, J.; Samant, M.G.; Parkin, S.S.P. Suppression of ionic liquid gate-induced metallization of SrTiO$_3$ (001) by oxygen. *Nano Lett.* **2013**, *13*, 4675–4678. https://doi.org/10.1021/nl402088f.

41. Zhang, L.; Zeng, S.; Yin, X.; Asmara, T.C.; Yang, P.; Han, K.; Cao, Y.; Zhou, W.; Wan, D.; Tang, C.S.; et al. The Mechanism of Electrolyte Gating on High-T$_c$ Cuprates: The Role of Oxygen Migration and Electrostatics. *ACS Nano* **2017**, *11*, 9950–9956. https://doi.org/10.1021/acsnano.7b03978.

42. Wei, Z.; Li, Q.; Gong, B.C.; Wei, X.; Hu, W.; Ni, Z.; He, G.; Qin, M.; Kusmartseva, A.; Kusmartsev, F.V.; et al. Two superconductor-insulator phase transitions in the spinel oxide Li$_{1\pm x}$Ti$_2$O$_{4-\delta}$ induced by ionic liquid gating. *Phys. Rev. B* **2021**, *103*, L140501. https://doi.org/10.1103/PhysRevB.103.L140501.

43. Petach, T.A.; Lee, M.; Davis, R.C.; Mehta, A.; Goldhaber-Gordon, D. Mechanism for the large conductance modulation in electrolyte-gated thin gold films. *Phys. Rev. B* **2014**, *90*, 081108. https://doi.org/10.1103/PhysRevB.90.081108.

44. Wang, X.; Zhang, S.; Fu, H.; Gao, M.; Ren, Z.; Chen, G. Dominant role of processing temperature in electric field induced superconductivity in layered ZrNBr. *New J. Phys.* **2019**, *21*, 023002. https://doi.org/10.1088/1367-2630/ab00c1.

45. Zakhidov, D.; Rehn, D.A.; Reed, E.J.; Salleo, A. Reversible electrochemical phase change in monolayer to bulk-like MoTe$_2$ by ionic liquid gating. *ACS Nano* **2020**, *14*, 2894–2903. https://doi.org/10.1021/acsnano.9b07095.

46. Radisavljevic, B.; Kis, A. Mobility engineering and a metal-insulator transition in monolayer MoS$_2$. *Nat. Mater.* **2013**, *12*, 815–820. https://doi.org/10.1038/nmat3687.

47. Wu, Z.; Xu, S.; Lu, H.; Khamoshi, A.; Liu, G.B.; Han, T.; Wu, Y.; Lin, J.; Long, G.; He, Y.; et al. Even–odd layer-dependent magnetotransport of high-mobility Q-valley electrons in transition metal disulfides. *Nat. Commun.* **2016**, *7*, 12955. https://doi.org/10.1038/ncomms12955.

48. Piatti, E.; Arbab, A.; Galanti, F.; Carey, T.; Anzi, L.; Spurling, D.; Roy, A.; Zhussupbekova, A.; Patel, K.A.; Kim, J.M.; et al. Charge transport mechanisms in inkjet-printed thin-film transistors based on two-dimensional materials. *Nat. Electron.* **2021**, *4*, 893–905. https://doi.org/10.1038/s41928-021-00684-9.

49. Biscaras, J.; Chen, Z.; Paradisi, A.; Shukla, A. Onset of two-dimensional superconductivity in space charge doped few-layer molybdenum disulfide. *Nat. Commun.* **2015**, *6*, 8826. https://doi.org/10.1038/ncomms9826.

50. Costanzo, D.; Zhang, H.; Reddy, B.A.; Berger, H.; Morpurgo, A.F. Tunnelling spectroscopy of gate-induced superconductivity in MoS$_2$. *Nat. Nanotechnol.* **2018**, *13*, 483–488. https://doi.org/10.1038/s41565-018-0122-2.

51. Zhang, R.; Tsai, I.L.; Chapman, J.; Khestanova, E.; Waters, J.; Grigorieva, I.V. Superconductivity in potassium-doped metallic polymorphs of MoS$_2$. *Nano Lett.* **2016**, *16*, 629–636. https://doi.org/10.1021/acs.nanolett.5b04361.

52. Bin Subhan, M.K.; Suleman, A.; Moore, G.; Phu, P.; Hoesch, M.; Kurebayashi, H.; Howard, C.A.; Schofield, S.R. Charge density waves in electron-doped molybdenum disulfide. *Nano Lett.* **2021**, *21*, 5516–5521. https://doi.org/10.1021/acs.nanolett.1c00677.

53. Enyashin, A.N.; Seifert, G. Density-functional study of Li$_x$MoS$_2$ intercalates ($0 \leq x \leq 1$). *Comput. Theor. Chem.* **2012**, *999*, 13–20. https://doi.org/10.1016/j.comptc.2012.08.005.

54. Zhuang, H.L.; Johannes, M.D.; Singh, A.K.; Hennig, R.G. Doping-controlled phase transitions in single-layer MoS$_2$. *Phys. Rev. B* **2017**, *96*, 165305. https://doi.org/10.1103/PhysRevB.96.165305.

55. Chen, X.; Chen, Z.; Li, J. Critical electronic structures controlling phase transitions induced by lithium ion intercalation in molybdenum disulphide. *Chin. Sci. Bull.* **2013**, *58*, 1632–1641. https://doi.org/10.1007/s11434-013-5834-y.

56. Rösner, M.; Haas, S.; Wehling, T.O. Phase diagram of electron-doped dichalcogenides. *Phys. Rev. B* **2014**, *90*, 245105. https://doi.org/10.1103/PhysRevB.90.245105.

57. Guo, Y.; Sun, D.; Ouyang, B.; Raja, A.; Song, J.; Heinz, T.F.; Brus, L.E. Probing the dynamics of the metallic-to-semiconducting structural phase transformation in MoS$_2$ crystals. *Nano Lett.* **2015**, *15*, 5081–5088. https://doi.org/10.1021/acs.nanolett.5b01196.

58. Voiry, D.; Mohite, A.; Chhowalla, M. Phase engineering of transition metal dichalcogenides. *Chem. Soc. Rev.* **2015**, *44*, 2702–2712. https://doi.org/10.1039/C5CS00151J.

59. Leng, K.; Chen, Z.; Zhao, X.; Tang, W.; Tian, B.; Nai, C.T.; Zhou, W.; Loh, K.P. Phase restructuring in transition metal dichalcogenides for highly stable energy storage. *ACS Nano* **2016**, *10*, 9208–9215. https://doi.org/10.1021/acsnano.6b05746.

60. Xia, J.; Wang, J.; Chao, D.; Chen, Z.; Liu, Z.; Kuo, J.L.; Yan, J.; Shen, Z.X. Phase evolution of lithium intercalation dynamics in 2*H*-MoS$_2$. *Nanoscale* **2017**, *9*, 7533–7540. https://doi.org/10.1039/C7NR02028G.

61. Boeri, L.; Hennig, R.G.; Hirschfeld, P.J.; Profeta, G.; Sanna, A.; Zurek, E.; Pickett, W.E.; Amsler, M.; Dias, R.; Eremets, M.; et al. The 2021 room-temperature superconductivity roadmap. *J. Phys. Condens. Matter* **2021**, *34*, 183002. https://doi.org/10.1088/1361-648X/ac2864.

62. Cui, Y.; Hu, Z.; Zhang, J.S.; Ma, W.L.; Ma, M.W.; Ma, Z.; Wang, C.; Yan, J.Q.; Sun, J.P.; Cheng, J.G.; et al. Ionic-Liquid-Gating Induced Protonation and Superconductivity in FeSe, FeSe$_{0.93}$S$_{0.07}$, ZrNCl, 1*T*-TaS$_2$ and Bi$_2$Se$_3$. *Chin. Phys. Lett.* **2019**, *36*, 077401. https://doi.org/10.1088/0256-307X/36/7/077401.

63. Rafique, M.; Feng, Z.; Lin, Z.; Wei, X.; Liao, M.; Zhang, D.; Jin, K.; Xue, Q.K. Ionic liquid gating induced protonation of electron-doped cuprate superconductors. *Nano Lett.* **2019**, *19*, 7775–7780. https://doi.org/10.1021/acs.nanolett.9b02776.

64. Meng, Y.; Xing, X.; Yi, X.; Li, B.; Zhou, N.; Li, M.; Zhang, Y.; Wei, W.; Feng, J.; Terashima, K.; et al. Protonation-induced discrete superconducting phases in bulk FeSe single crystals. *Phys. Rev. B* **2022**, *105*, 134506. https://doi.org/10.1103/PhysRevB.105.134506.

65. Wang, J.; Li, Q.; Xie, W.; Chen, G.; Zhu, X.; Wen, H.H. Superconductivity at 44.4 K achieved by intercalating EMIM+ into FeSe. *Chin. Phys. B* **2021**, *30*, 107402. https://doi.org/10.1088/1674-1056/ac1f09.

66. Shi, M.; Wang, N.; Lei, B.; Ying, J.; Zhu, C.; Sun, Z.; Cui, J.; Meng, F.; Shang, C.; Ma, L.; et al. FeSe-based superconductors with a superconducting transition temperature of 50 K. *New J. Phys.* **2018**, *20*, 123007. https://doi.org/10.1088/1367-2630/aaf312.

67. Xu, H.S.; Wu, S.; Zheng, H.; Yin, R.; Li, Y.; Wang, X.; Tang, K. Research Progress of FeSe-based Superconductors Containing Ammonia/Organic Molecules Intercalation. *Top. Curr. Chem.* **2022**, *380*, 11. https://doi.org/10.1007/s41061-022-00368-8.

68. Nečas, D.; Klapetek, P. Gwyddion: An open-source software for SPM data analysis. *Cent. Eur. J. Phys.* **2012**, *10*, 181–188. https://doi.org/10.2478/s11534-011-0096-2.

69. Qiu, H.; Xu, T.; Wang, Z.; Ren, W.; Nan, H.; Ni, Z.; Chen, Q.; Yuan, S.; Miao, F.; Song, F.; et al. Hopping transport through defect-induced localized states in molybdenum disulphide. *Nat. Commun.* **2013**, *4*, 2642. https://doi.org/10.1038/ncomms3642.

70. Lee, C.; Yan, H.; Brus, L.E.; Heinz, T.F.; Hone, J.; Ryu, S. Anomalous lattice vibrations of single-and few-layer MoS$_2$. *ACS Nano* **2010**, *4*, 2695–2700. https://doi.org/10.1021/nn1003937.

71. Chakraborty, B.; Bera, A.; Muthu, D.; Bhowmick, S.; Waghmare, U.V.; Sood, A.K. Symmetry-dependent phonon renormalization in monolayer MoS$_2$ transistor. *Phys. Rev. B* **2012**, *85*, 161403. https://doi.org/10.1103/PhysRevB.85.161403.

72. Lu, X.; Utama, M.I.B.; Wang, X.; Xu, W.; Zhao, W.; Owen, M.H.S.; Xiong, Q. Gate-Tunable resonant Raman spectroscopy of bilayer MoS$_2$. *Small* **2017**, *13*, 1701039. https://doi.org/10.1002/smll.201701039.

73. Chen, X.; Berner, N.C.; Backes, C.; Duesberg, G.S.; McDonald, A.R. Functionalization of Two-Dimensional MoS$_2$: On the Reaction Between MoS$_2$ and Organic Thiols. *Angew. Chem.* **2016**, *128*, 5897–5902. https://doi.org/10.1002/anie.201510219.

74. Höfft, O.; Bahr, S.; Kempter, V. Investigations with infrared spectroscopy on films of the ionic liquid [EMIM]Tf2N. *Langmuir* **2008**, *24*, 11562–11566. https://doi.org/10.1021/la802045j.

75. Boumediene, M.; Haddad, B.; Paolone, A.; Drai, M.; Villemin, D.; Rahmouni, M.; Bresson, S.; Abbas, O. Synthesis, thermal stability, vibrational spectra and conformational studies of novel dicationic meta-xylyl linked bis-1-methylimidazolium ionic liquids. *J. Mol. Struct.* **2019**, *1186*, 68–79. https://doi.org/10.1016/j.molstruc.2019.03.019.

76. Heimer, N.E.; Del Sesto, R.E.; Meng, Z.; Wilkes, J.S.; Carper, W.R. Vibrational spectra of imidazolium tetrafluoroborate ionic liquids. *J. Mol. Liq.* **2006**, *124*, 84–95. https://doi.org/10.1016/j.molliq.2005.08.004.

77. Prater, C.; Kjoller, K.; Shetty, R. Nanoscale infrared spectroscopy. *Mater. Today* **2010**, *13*, 56–60. https://doi.org/10.1016/S1369-7021(10)70205-4.

78. Dazzi, A.; Prater, C.B. AFM-IR: Technology and applications in nanoscale infrared spectroscopy and chemical imaging. *Chem. Rev.* **2017**, *117*, 5146–5173. https://doi.org/10.1021/acs.chemrev.6b00448.

79. Melitz, W.; Shen, J.; Kummel, A.C.; Lee, S. Kelvin probe force microscopy and its application. *Surf. Sci. Rep.* **2011**, *66*, 1–27. https://doi.org/10.1016/j.surfrep.2010.10.001.

80. Almadori, Y.; Bendiab, N.; Grevin, B. Multimodal Kelvin probe force microscopy investigations of a photovoltaic WSe$_2$/MoS$_2$ type-II interface. *ACS Appl. Mater. Interfaces* **2018**, *10*, 1363–1373. https://doi.org/10.1021/acsami.7b14616.

81. Ding, S.; Xiao, X.; Liu, S.; Wu, J.; Huang, Z.; Qi, X.; Li, J. Detection of interfacial charge transfer in MoS$_2$/PbI$_2$ heterostructures via Kelvin probe force microscope. *Appl. Phys. A* **2019**, *125*, 287. https://doi.org/10.1007/s00339-019-2578-9.

82. Chen, Q.H.; Lu, J.M.; Liang, L.; Zheliuk, O.; Ali, A.; Sheng, P.; Ye, J.T. Inducing and Manipulating Heteroelectronic States in a Single MoS$_2$ Thin Flake. *Phys. Rev. Lett.* **2017**, *119*, 147002. https://doi.org/10.1103/PhysRevLett.119.147002.

83. Gallagher, P.; Lee, M.; Petach, T.A.; Stanwyck, S.W.; Williams, J.R.; Watanabe, K.; Taniguchi, T.; Goldhaber-Gordon, D. A high-mobility electronic system at an electrolyte-gated oxide surface. *Nat. Commun.* **2015**, *6*, 6437. https://doi.org/10.1038/ncomms7437.

84. Saito, Y.; Iwasa, Y. Ambipolar insulator-to-metal transition in black phosphorus by ionic-liquid gating. *ACS Nano* **2015**, *9*, 3192–3198. https://doi.org/10.1021/acsnano.5b00497.

85. Piatti, E.; Galasso, S.; Tortello, M.; Nair, J.; Gerbaldi, C.; Bruna, M.; Borini, S.; Daghero, D.; Gonnelli, R.S. Carrier mobility and scattering lifetime in electric double-layer gated few-layer graphene. *Appl. Surf. Sci.* **2017**, *395*, 37–41. https://doi.org/10.1016/j.apsusc.2016.06.192.

86. Gonnelli, R.S.; Piatti, E.; Sola, A.; Tortello, M.; Dolcini, F.; Galasso, S.; Nair, J.R.; Gerbaldi, C.; Cappelluti, E.; Bruna, M.; et al. Weak localization in electric-double-layer gated few-layer graphene. *2D Mater.* **2017**, *4*, 035006. https://doi.org/10.1088/2053-1583/aa5afe.

87. Piatti, E.; Hatano, T.; Daghero, D.; Galanti, F.; Gerbaldi, C.; Guastella, S.; Portesi, C.; Nakamura, I.; Fujimoto, R.; Iida, K.; et al. Ambipolar suppression of superconductivity by ionic gating in optimally doped BaFe$_2$(As,P)$_2$ ultrathin films. *Phys. Rev. Mater.* **2019**, *3*, 044801. https://doi.org/10.1103/PhysRevMaterials.3.044801.

88. Ovchinnikov, D.; Gargiulo, F.; Allain, A.; Pasquier, D.J.; Dumcenco, D.; Ho, C.H.; Yazyev, O.V.; Kis, A. Disorder engineering and conductivity dome in ReS$_2$ with electrolyte gating. *Nat. Commun.* **2016**, *7*, 12391. https://doi.org/10.1038/ncomms12391.

89. Lu, J.; Zheliuk, O.; Chen, Q.; Leermakers, I.; Hussey, N.E.; Zeitler, U.; Ye, J. Full superconducting dome of strong Ising protection in gated monolayer WS$_2$. *Proc. Natl. Acad. Sci. USA* **2018**, *115*, 3551–3556. https://doi.org/10.1073/pnas.1716781115.

90. Qin, M.; Ding, D.; Li, S.; Han, X.; Niu, R.; Yin, D.; Qu, Z.; Watanabe, K.; Taniguchi, T.; Liao, Z.M.; et al. Probing the nature of an emergent insulator in ionic gated monolayer transition metal dichalcogenides. *Preprint.* https://doi.org/10.21203/rs.3.rs-95219/v1.

91. Gor'kov, L.P.; Grüner, G. *Charge Density Waves in Solids*; North Holland, The Netherlands, 1989.

92. Rossnagel, K. On the origin of charge-density waves in select layered transition-metal dichalcogenides. *J. Phys. Condens. Matter* **2011**, *23*, 213001. https://doi.org/10.1088/0953-8984/23/21/213001.

93. Zhu, X.; Cao, Y.; Zhang, J.; Plummer, E.; Guo, J. Classification of charge density waves based on their nature. *Proc. Natl. Acad. Sci. USA* **2015**, *112*, 2367–2371. https://doi.org/10.1073/pnas.1424791112.

94. Morosan, E.; Zandbergen, H.W.; Dennis, B.; Bos, J.; Onose, Y.; Klimczuk, T.; Ramirez, A.; Ong, N.; Cava, R.J. Superconductivity in Cu$_x$TiSe$_2$. *Nat. Phys.* **2006**, *2*, 544–550. https://doi.org/10.1038/nphys360.

95. Bhoi, D.; Khim, S.; Nam, W.; Lee, B.; Kim, C.; Jeon, B.G.; Min, B.; Park, S.; Kim, K.H. Interplay of charge density wave and multiband superconductivity in 2H-Pd$_x$TaSe$_2$. *Sci. Rep.* **2016**, *6*, 24068. https://doi.org/10.1038/srep24068.

96. Fang, L.; Wang, Y.; Zou, P.Y.; Tang, L.; Xu, Z.; Chen, H.; Dong, C.; Shan, L.; Wen, H.H. Fabrication and superconductivity of Na$_x$TaS$_2$ crystals. *Phys. Rev. B* **2005**, *72*, 014534. https://doi.org/10.1103/PhysRevB.72.014534.

97. Cao, Z.Y.; Hu, J.W.; Goncharov, A.F.; Chen, X.J. Nontrivial metallic state of MoS$_2$. *Phys. Rev. B* **2018**, *97*, 214519. https://doi.org/10.1103/PhysRevB.97.214519.

98. Costanzo, D.; Jo, S.; Berger, H.; Morpurgo, A.F. Gate-induced superconductivity in atomically thin MoS$_2$ crystals. *Nat. Nanotechnol.* **2016**, *11*, 339–344. https://doi.org/10.1038/nnano.2015.314.

99. Fu, Y.; Liu, E.; Yuan, H.; Tang, P.; Lian, B.; Xu, G.; Zeng, J.; Chen, Z.; Wang, Y.; Zhou, W.; et al. Gated tuned superconductivity and phonon softening in monolayer and bilayer MoS$_2$. *NPJ Quant. Mater.* **2017**, *2*, 52. https://doi.org/10.1038/s41535-017-0056-1.

100. Wu, H.; Li, S.; Susner, M.; Kwon, S.; Kim, M.; Haugan, T.; Lv, B. Spacing dependent and cation doping independent superconductivity in intercalated 1T 2D SnSe$_2$. *2D Mater.* **2019**, *6*, 045048. https://doi.org/10.1088/2053-1583/ab3ea1.

101. Ma, L.; Shi, M.; Kang, B.; Peng, K.; Meng, F.; Zhu, C.; Cui, J.; Sun, Z.; Ma, D.; Wang, H.; et al. Quasi-two-dimensional superconductivity in SnSe$_2$ via organic ion intercalation. *Phys. Rev. Mater.* **2020**, *4*, 124803. https://doi.org/10.1103/PhysRevMaterials.4.124803.